2D graphene oxide films expand functionality of photonic chips

Supplementary Information

Jiayang Wu[1,], Yuning Zhang[1,2], Junkai Hu[1,3], Yunyi Yang[1], Di Jin[1,3], Wenbo Liu[4,5], Duan Huang[3], Baohua Jia[4,5*], David J. Moss[1,*]*

[1]Optical Sciences Centre, Swinburne University of Technology, Hawthorn, VIC 3122, Australia.

[2]School of Physics, Peking University, Haidian District, Beijing, China,100871

[3]School of Computer Science and Engineering, Central South University, Changsha 410083, China

[4]Centre for Atomaterials and Nanomanufacturing, School of Science, RMIT University, Melbourne, VIC 3000, Australia

[5]Australian Research Council (ARC) Industrial Transformation Training, Centre in Surface Engineering for Advanced Materials (SEAM), RMIT University, Melbourne, Victoria 3000, Australia

*E-mail: *jiayangwu@swin.edu.au, baohua.jia@rmit.edu.au, dmoss@swin.edu.au*

Number of notes: 17

Number of figures & tables: 17

Number of equations: 26

This supplementary information includes the following sections:

Supplementary Note 1: Setup for pump-probe experiment

We used the experimental setup shown in **Fig. S1** to demonstrate the control of the loss of a low-power probe light using a high-power pump light. The pump and the probe at different wavelengths were generated by two tunable continuous-wave (CW) lasers. The pump was amplified by an erbium-doped fiber amplifier (EDFA), followed by a bandpass filter (BPF) to suppress the amplified spontaneous emission (ASE) noise. A variable optical attenuator (VOA) was employed to adjust the power of the pump light. The pump and the probe were combined by a 50:50 coupler before sent to the device under test (DUT). Both of them were adjusted to TE polarization using two polarization controllers (PCs). An optical isolator was inserted before the DUT to prevent damages induced by the reflected light. The output from the DUT went through another BPF to remove the pump, and the remaining probe was sent to an optical power meter (OPM). In our experiment, the wavelength tuning range for the high-power pump was constrained by the operation bandwidth of the EDFA in **Fig. S1**, which was capable of effectively amplifying signals only within the telecom C band.

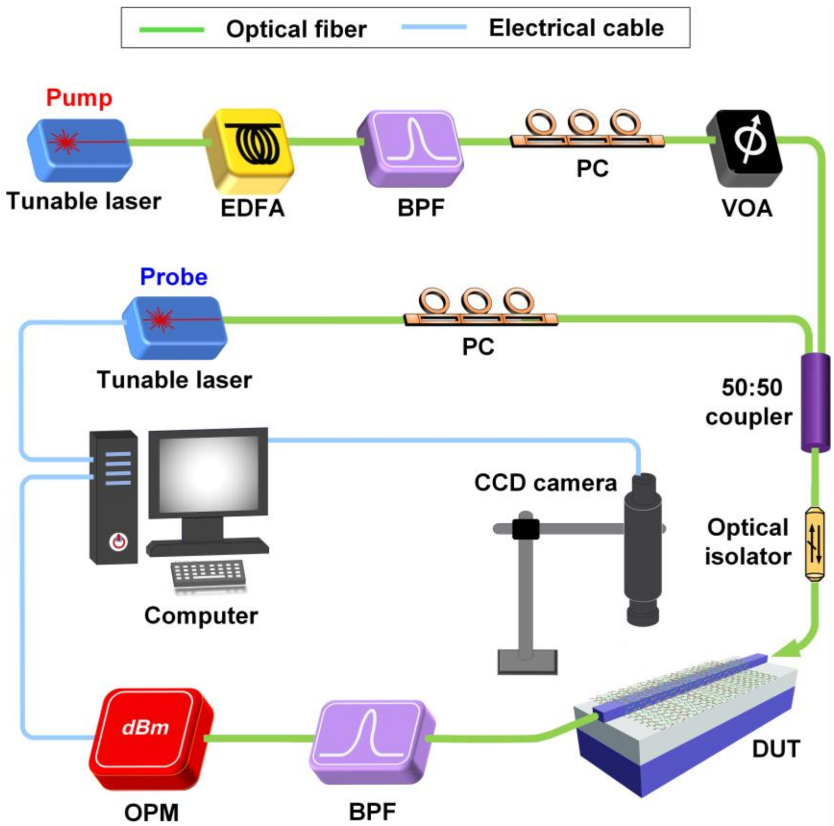

Fig. S1 | Experimental setup for the pump-probe experiment. EDFA: erbium doped fiber amplifier. BPF:

band pass filter. PC: polarization controller. VOA: variable optical attenuator. DUT: device under test. CCD: charged-coupled device. OPM: optical power meter.

Supplementary Note 2: Influence of two-photon absorption (TPA) and free carrier absorption (FCA) in Si waveguides

According to the theory in Ref. [1], the loss induced by the TPA and FCA in Si waveguides can be calculated based on

$$\alpha_{TPA\text{-}Si} + \alpha_{FCA\text{-}Si} = \frac{\beta_{TPA\text{-}Si}}{A_{eff}} |A(z, t)|^2 + \sigma N_{c\text{-}Si} \tag{S1}$$

where $\beta_{TPA\text{-}Si} = 5 \times 10^{-12}$ m/W and $\sigma = 1.45 \times 10^{-21}$ m^2 are the TPA and FCA coefficients of Si, respectively [2]. $A(z, t)$ is the slowly varying temporal envelope of optical field propagation along the waveguide (*i.e.*, z axis). A_{eff} is the effective mode area given by [3]

$$A_{eff} = \frac{\left(\iint_D S_z dxdy\right)^2}{\iint_D S_z^2 dxdy} \tag{S2}$$

where D is the integral domain over the different material regions with optical fields, S_z is the time-averaged Poynting vector calculated using FDTD mode simulation software. In **Eq. (S1)**, $N_{c\text{-}Si}$ is the free carrier density given by [1]:

$$\frac{\partial N_{c\text{-}Si}(z,t)}{\partial t} = \frac{\beta_{TPA\text{-}Si}}{2\hbar\omega} \cdot \frac{|A(z,t)|^4}{A_{eff}^2} - \frac{N_{c\text{-}Si}(z,t)}{\tau_c} \tag{S3}$$

where $\hbar$ is Planck's constant, ω is the angular frequency, and τ_c = ~1 ns is the effective carrier lifetime. For CW light and once it attains a stable thermal equilibrium state, $N_{c\text{-}Si}$ remains constant over time. Consequently, the expression on the left-hand side of **Eq. (S3)** equals to zero.

Fig. S2 shows the excess propagation loss (PL) of the uncoated Si waveguide induced by TPA and FCA, which was calculated based on **Eqs. (S1) – (S3)** and plotted as a function of input power. As observed, at an input power of 25 dBm, the excess PL remains below 0.03 dB/mm. This implies that the additional insertion loss caused by TPA and FCA for Si waveguides with a length of ~3.0 mm in our experiments was < 0.1 dB. In fact, given that the light power decreases along the waveguide, the additional insertion loss caused by TPA and FCA was even smaller than 0.03 dB/mm × 3 mm = 0.09 dB. The results reflect that the loss induced by TPA and FCA of Si was negligible within the power range we investigated.

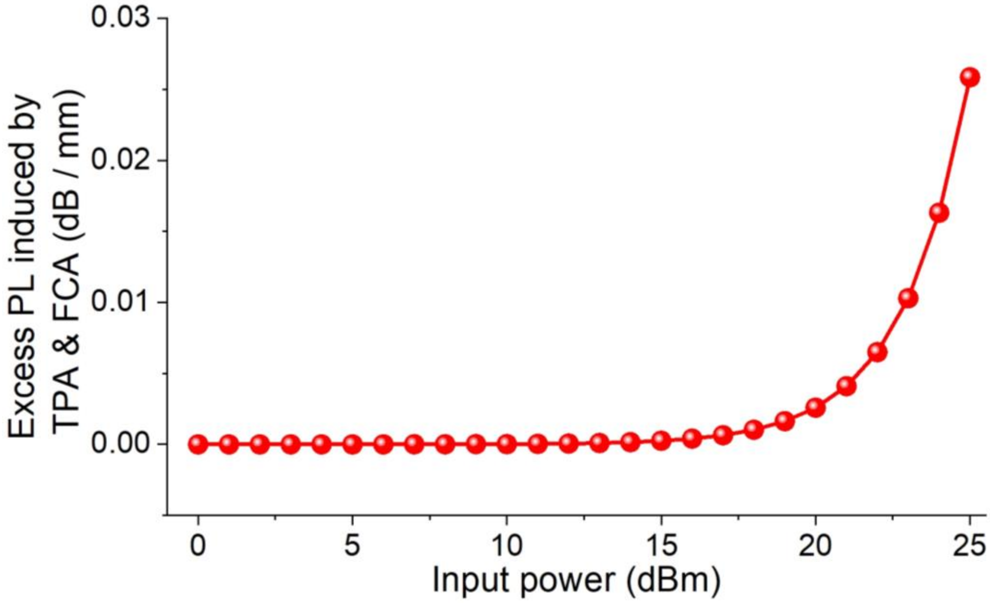

Fig. S2 | Excess propagation loss (PL) induced by TPA and FCA in Si waveguide as a function of input power.

Supplementary Note 3: Raman spectra of photo-thermally reduced GO

To verify that there was reduction of GO induced by the photo-thermal effects, we measured the Raman spectra of a monolayer of GO coated on a Si waveguide after injecting different input CW powers, as shown in **Fig. S3**. The Raman spectra were recorded at the start of the GO coated segment, where the light power coupled into the GO film was the highest. After applying an input power of P_{in} =19.2 dBm, the measured Raman spectrum did not show any obvious difference compared to that obtained at the initial state without light injection. This indicates that the GO film did not have permanent changes in its properties at this power level. In contrast, a slight decrease in the intensity ratio of the *D* to *G* peaks (I_D / I_G) was observed in the measured Raman spectrum for P_{in} = ~21.0 dBm, and an even lower I_D / I_G was observed in the measured Raman spectrum for P_{in} = ~22.5 dBm. This reflects that there was permanent reduction of the GO film after tuning off the input light, and a higher degree of reduction can be achieved by increasing the applied input power. We note that the decrease in I_D / I_G is similar to that observed in Refs. [4, 5] , and can be attributed to the removal of the OCFGs due to the photo-thermal effects as well as the partial restoration of the sp^2 carbon network.

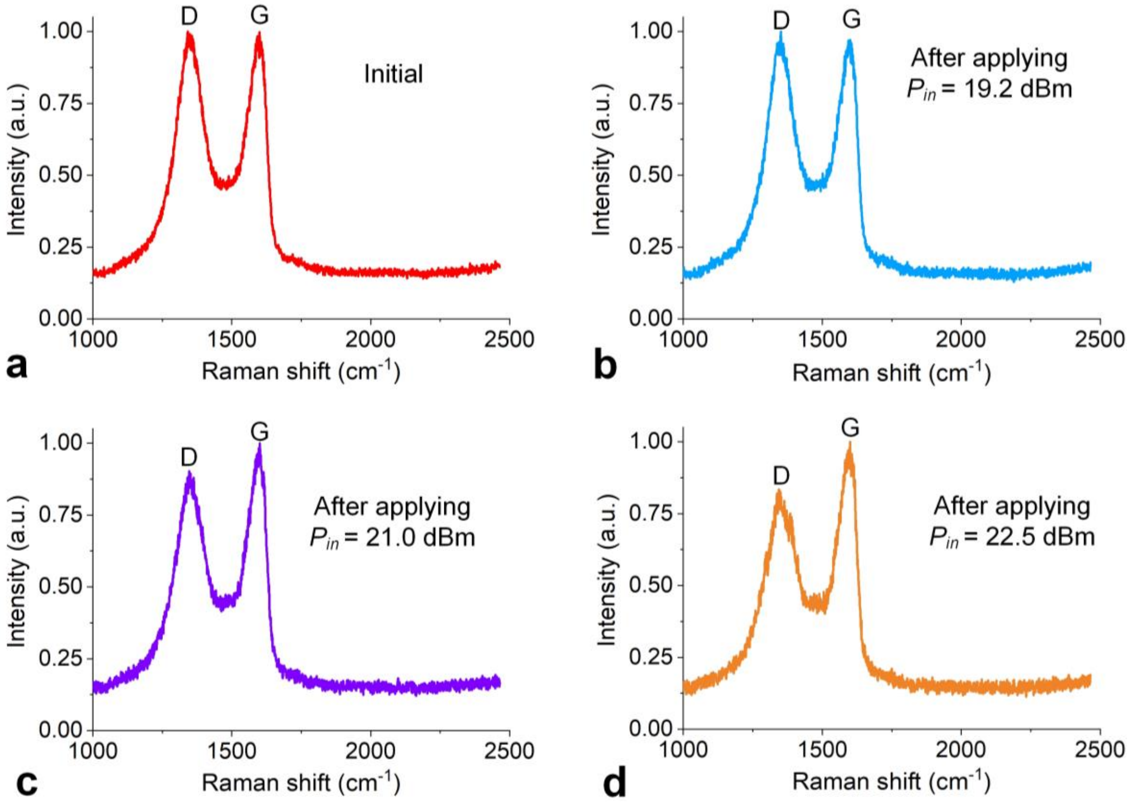

Fig. S3 | Measured Raman spectra of a monolayer of GO coated on a Si waveguide after applying different input CW powers (P_{in}). **a.** Initial state without applying light power. **b.** After applying P_{in} = ~19.2 dBm. **c.** After applying P_{in} = ~21.0 dBm. **d.** After applying P_{in} = ~22.5 dBm. The Raman spectra were recorded at the start of the GO coated segment.

Supplementary Note 4: Setup for on-off switching experiment

Fig. S4 shows the experimental setup used in our on-off switching experiment, which was modified based on the experimental setup in **Fig. S1**. The CW pump light was first modulated by a Mach-Zehnder modulator (MZM), which was driven by a ~1-ms square electrical signal with a pattern of "10000000" generated by an arbitrary waveform generator (AWG). The MZM was biased at quadrature point of the transmission curve [6]. The modulated pump was then amplified to a power of ~19 dBm using an EDFA, with a BPF inserted afterwards to suppress the ASE noise. Following this, the pump and the probe were combined by a 50:50 coupler and sent to the DUT. PCs were employed to adjust the input polarizations for polarization-sensitive components such as the MZM and the DUT. After going through the DUT, the probe signal was isolated from the pump light using a BPF and subsequently directed into an oscilloscope for the observation of temporal waveforms.

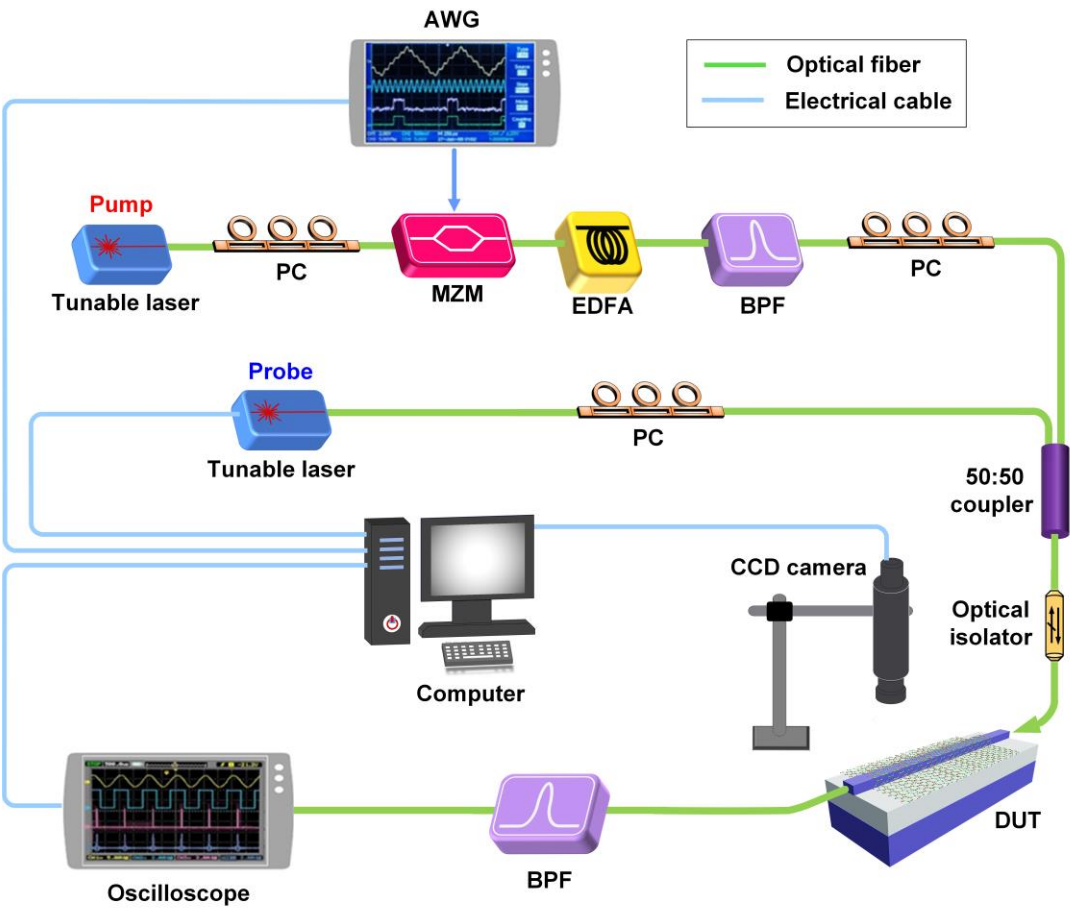

Fig. S4 | Experimental setup for the on-off switching experiment. PC: polarization controller. MZM: Mach-Zehnder Modulator. AWG: arbitrary waveform generator. EDFA: erbium doped fiber amplifier. BPF: band pass filter. DUT: device under test. CCD: charged-coupled device.

Supplementary Note 5: Time constants for the photo-thermal response in GO

The rising time constant for the photo-thermal response in **Fig. 3g** was obtained by fitting the rising edge in the temporal waveform of the output probe light with

$$I(t) = I_{max} - (I_{max} - I_{min})\, exp\, [(t - t_r)/c_r] \quad \text{(S4)}$$

where $I(t)$ is the intensity of the temporal waveform, which is a function of time t. I_{max} and I_{min} are the maximum and minimum intensities corresponding to the on and off states, respectively. t_r is the time at which the intensity starts to rise and c_r is the rising time constant.

Similarly, the falling time constant was obtained by fitting the falling edge in the temporal waveform of the output probe light with

$$I(t) = I_{max}\, exp\, [(t - t_f)/c_f] \quad \text{(S5)}$$

where t_f is the time at which the intensity starts to fall and c_f is the falling time constant.

The obtained c_r and c_f are ~52 μs and ~98 μs, respectively. These values indicate the time intervals during which the waveform intensity increases or decreases to reach a level corresponding to $1/e$ of the maximum variation [7].

Supplementary Note 6: Setup for demonstration of optical power limiting

We used the experimental setup shown in **Fig. S5** to test the optical power limiting performance of GO-coated Si waveguides. In contrast to the experimental setups in **Figs. S1** and **S4**, there was only a single input CW light, which was amplified by an EDFA, followed by a BPF to suppress the ASE noise. A PC and a VOA were employed to adjust the polarization and power of the input light before injecting it into the DUT, respectively. The output from the DUT was sent to an OPM for measuring its power.

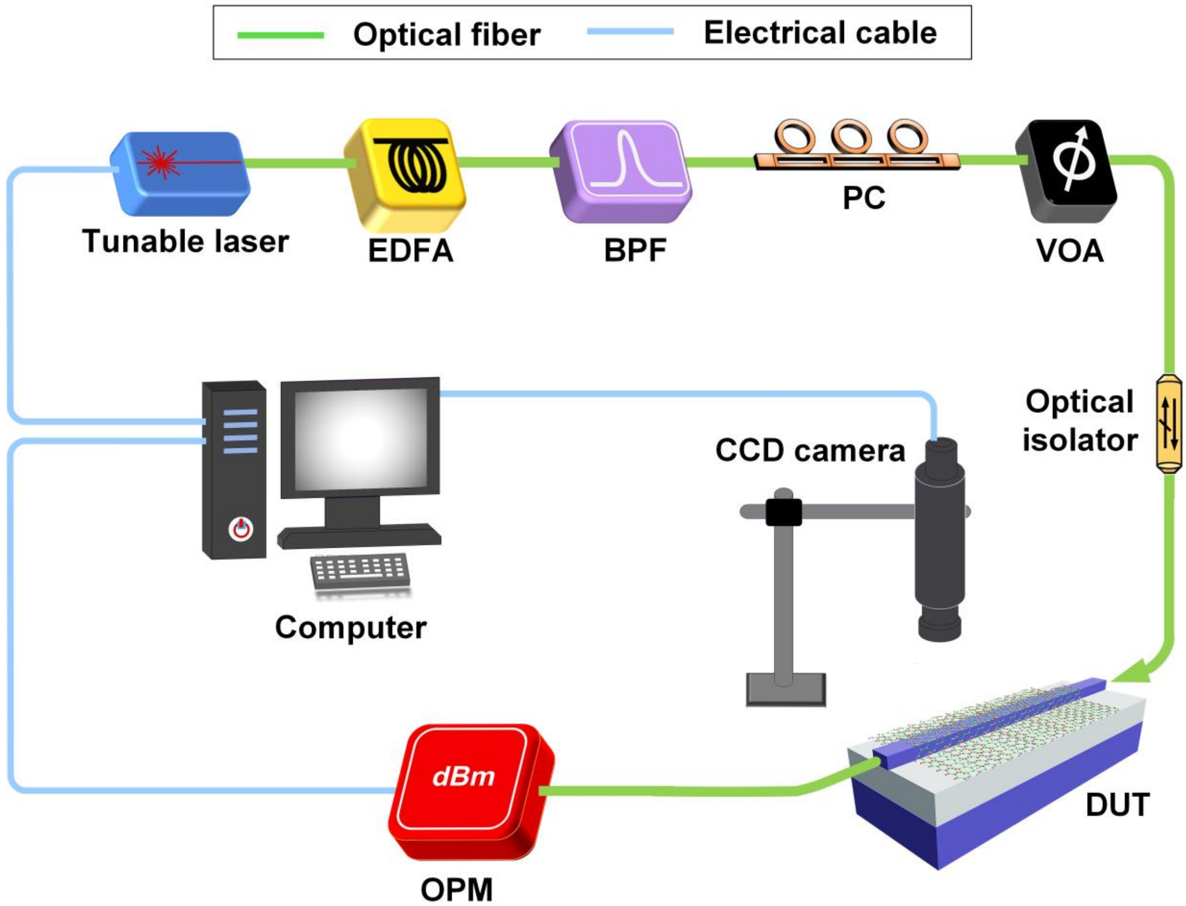

Fig. S5 | Experimental setup for demonstration of optical power limiting. EDFA: erbium doped fiber amplifier. BPF: band pass filter. PC: polarization controller. VOA: variable optical attenuator. DUT: device under test. CCD: charged-coupled device. OPM: optical power meter.

Supplementary Note 7: Performance comparison of different waveguide configurations

In order to optimize the device performance, we compared the loss changes induced by the photo-thermal effects in different waveguide configurations. As illustrated in **Fig. S6a**, we fabricated four different types of waveguides, including (I) uncoated Si waveguides, (II) Si waveguides coated with a polymer layer, (III) Si waveguides coated with a polymer layer and a monolayer of GO, and (IV) Si waveguides coated with a monolayer of GO sandwiched between two polymer layers. The order of these four waveguides also aligns with the sequence of film coating onto the Si waveguide surface during the self-assembly processes.

Fig. S6b shows the measured output power (P_{out}) versus input power (P_{in}) for a CW light propagation through waveguides I – IV, which reflects interesting insights into the photo-thermal effects in these waveguides. In contrast to waveguides III and IV, waveguides I and II did not show any obvious power limiting behaviour for P_{in} < 22 dBm. This reflects that the loss increase in this power range was induced by the GO film. Due to the limited endurability of the polymer at high temperatures, waveguides II – IV exhibited a rapid decrease in P_{out} when P_{in} exceeded a specific threshold, where the polymer suffered from significant thermal damage. Compared to waveguides III and IV, waveguide II had a higher power threshold for inducing significant thermal damage to the polymer layer. This could probably be attributed to the absence of GO, which had significantly increased temperatures at high power levels.

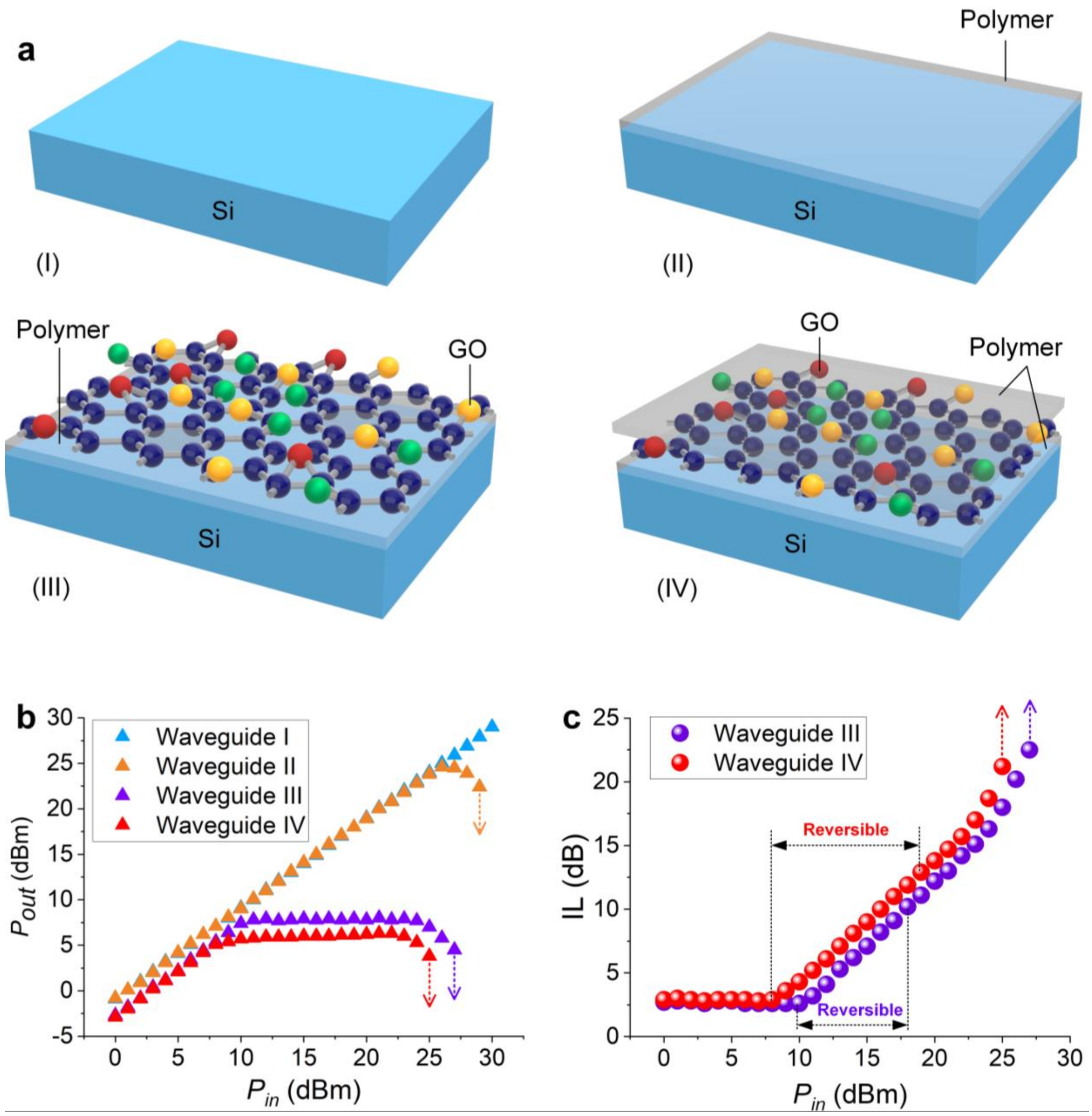

Fig. S6 | a. Schematic illustration of different types of waveguides, including (I) uncoated Si waveguide, (II) Si waveguide coated with a polymer layer, (III) Si waveguide coated with a polymer layer and a monolayer of GO, and (IV) Si waveguide coated with a monolayer of GO sandwiched between two polymer layers. **b.** Measured output power (P_{out}) versus input power (P_{in}) for a CW light propagation through waveguides I – IV in **a**. **c.** Insertion loss (IL) versus P_{in} for waveguides III and IV. The corresponding input power ranges for reversible photo-thermal changes are also indicated. In **b** and **c**, the arrows indicate a rapid decrease in P_{out} or increase in the IL once reaching the corresponding input power thresholds. The GO film coating length is L_c = 1.0 mm.

Fig. S6c shows the insertion loss (IL) of waveguides III and IV as a function of P_{in}, which was extracted from **Fig. S6b**. We also marked the input power ranges for reversible photo-thermal changes in these two waveguides. As can be seen, the range for waveguide IV is larger than that for waveguide III. More specifically, waveguide IV has a lower P_{thres1} (*i.e.*, the lower limit) and a higher P_{thres2} (*i.e.*, the upper limit). The former can be attributed to the diminished thermal dissipation within the polymer-coated GO layer, whereas the latter is due to the fact that the polymer cover layer can impede the release of the OCFGs into the surrounding air during the photo-thermal processes. The improved thermal dissipation in waveguide III is further evident through its higher power threshold for inducing thermal damage to the polymer layer.

For applications such as power limiting and non-reciprocal light transmission, a larger input power range for reversible photo-thermal changes is desirable. A larger power range, for example, facilitates a higher non-reciprocal transmission ratio (NTR). Consequently, we selected waveguide IV for our experimental demonstrations. On the other hand, for applications such as nonlinear optics, where low loss is essential to enhance nonlinear optical processes [8-10], waveguide III with relatively weak photo-thermal effects represents a more suitable option.

Supplementary Note 8: Performance comparison of TE and TM polarizations

In our previous work, we found that 2D GO films exhibited significant anisotropy in material absorption [11], which results in difference in the insertion loss of GO-coated integrated waveguides between TE and TM polarizations. Here, we compare the loss changes induced by photo-thermal effects in GO-Si waveguides for TE and TM polarizations. We measured the P_{thres1}, P_{thres2}, and P_{thres3} for both polarizations, using Si waveguides coated with a monolayer of GO and the same coating length of L_c = 1.0 mm. As illustrated in **Fig. 4c**, P_{thres1} and P_{thres2} correspond to the lower and upper limits of the input power range for inducing reversible photo-thermal changes, respectively, while P_{thres3} represents the input power threshold for inducing permanent thermal damage to the polymer layer.

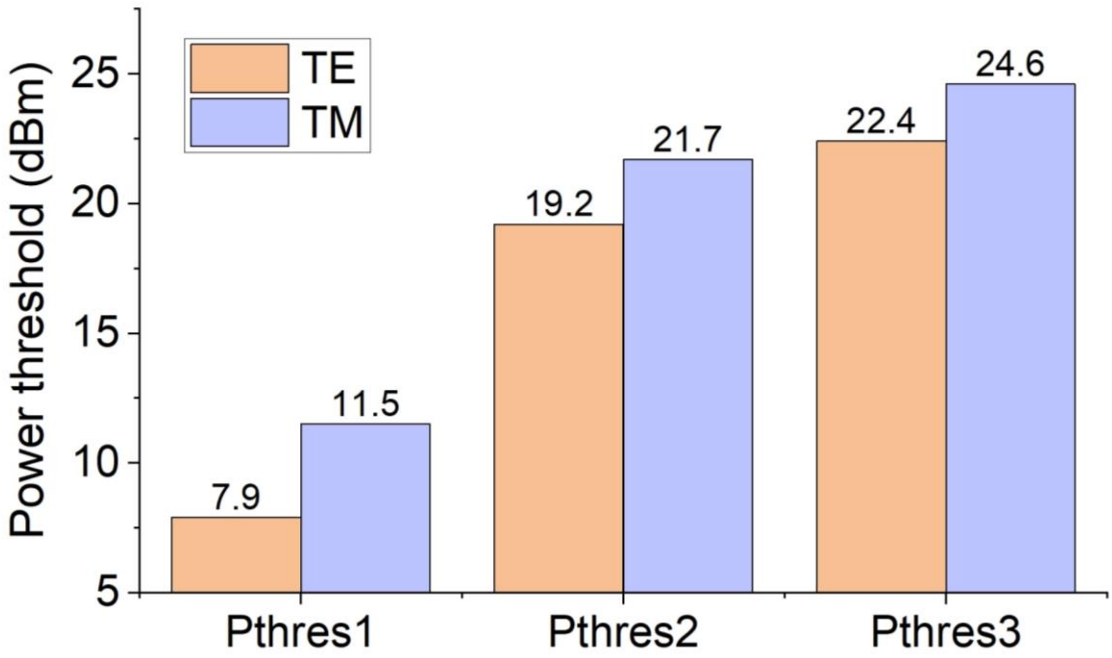

Fig. S7 | Measured P_{thres1}, P_{thres2}, and P_{thres3} for TE and TM polarizations in Si waveguide coated with a monolayer of GO (N = 1). The GO film coating length is L_c = 1.0 mm.

As shown in **Fig. S7**, TM polarization exhibits higher values for P_{thres1}, P_{thres2}, and P_{thres3} compared to TE polarization, indicating that the photo-thermal changes induced by a TM-polarized light are not as strong as those for a TE-polarized light. This is because TE polarization supports in-plane interaction between the waveguide's evanescent field and the 2D GO film, which is much stronger than the out-of-plane interaction for TM polarization [12].

Compared to TM polarization, TE polarization has a larger input power range for reversible photo-thermal changes, making it more suitable for applications such as power limiting and non-reciprocal light transmission. It is also interesting to note that, while the polymer layer does not exhibit significant anisotropy in light absorption, TE polarization has a lower value of P_{thres3}. This phenomenon is likely attributed to the increased heat exchange between the polymer layer and the GO layer with a higher temperature during the in-plane light-matter interaction.

Supplementary Note 9: Performance comparison of different waveguide geometries

We also compare the photo-thermal changes for GO-Si waveguides with different waveguide geometries. We measured the P_{thres1}, P_{thres2}, and P_{thres3} for GO-Si waveguides with the same height of 220 nm but different widths ranging from 400 nm to 600 nm. For comparison, all the hybrid waveguides were coated with a monolayer of GO, and the GO film coating length was kept the same as L_c = 1.0 mm. As shown in **Fig. S8a**, all of the P_{thres1}, P_{thres2}, and P_{thres3} exhibit a decrease as the waveguide width increases. This can be attributed to the increase in the mode overlap with the GO film on the waveguide top surface for a larger waveguide width, as indicated by the FDTD mode simulation results in **Fig. S8b**. These results also reflect that the waveguide width can be changed to achieve various P_{thres1}, P_{thres2}, and P_{thres3} values that meet different requirements in practical applications.

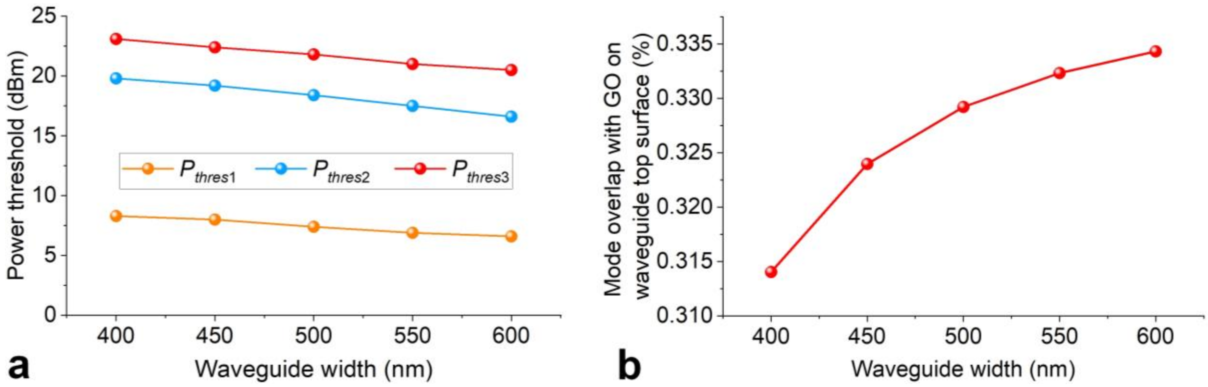

Fig. S8 | a. Measured P_{thres1}, P_{thres2}, and P_{thres3} for GO-Si waveguides with different waveguide widths. All the hybrid waveguides are coated with a monolayer of GO, and the GO film coating length is L_c = 1.0 mm. **b.** Mode overlap with GO on waveguide top surface versus waveguide width. The height of all the waveguides is 220 nm.

Supplementary Note 10: Setup for demonstration of non-reciprocal light transmission

Fig. S9 shows the experimental setup used for demonstration of non-reciprocal transmission for a CW light. The CW light generated by a tunable laser was amplified by an EDFA, followed by a BPF to suppress the ASE noise. The polarization and power of the light input into the DUT were adjusted by using a PC and a VOA, respectively. The output from the DUT was directed to an OPM for power measurement. Note that the orientations labeled as 'Forward' and 'Backward' in the DUT are consistent with those depicted in **Fig. 5a**. We also demonstrated non-reciprocal transmission of a 10-Gbit/s NRZ signal modulated onto a CW light. The experimental setup remained identical to that shown in **Fig. S9**, with the exception that the CW light was modulated using an MZM driven by a 10-Gbit/s NRZ signal generated by a pulse pattern generator.

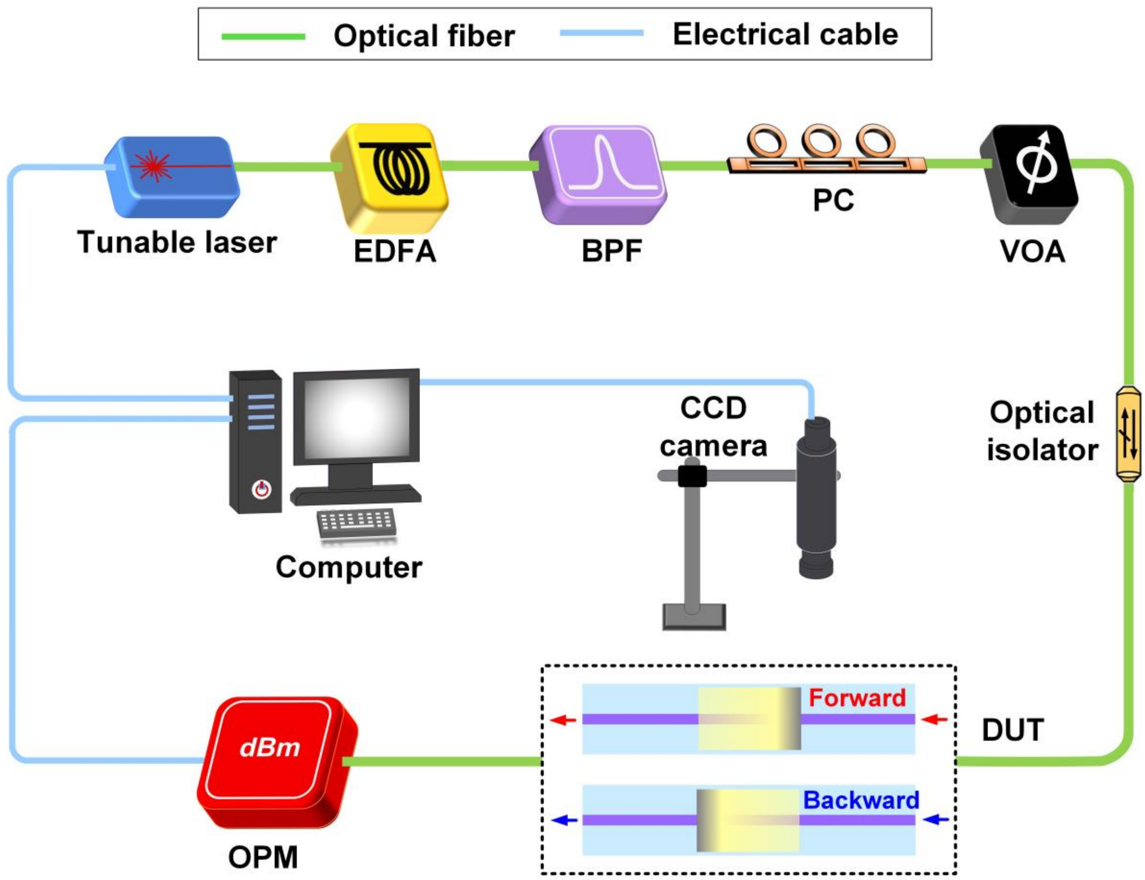

Fig. S9 | Experimental setup for demonstration of non-reciprocal light transmission. EDFA: erbium doped fiber amplifier. BPF: band pass filter. PC: polarization controller. VOA: variable optical attenuator. DUT: device under test. CCD: charged-coupled device. OPM: optical power meter.

Supplementary Note 11: Performance comparison of integrated non-reciprocal light transmission devices

In **Table S1**, we compare the performance of state-of-the-art integrated non-reciprocal light transmission devices. Various mechanisms have been proposed to realize non-reciprocal light transmission, such as magneto-optics [13, 14], thermo-optics [15, 16], synthetic magnetic [17, 18], acousto-optics [19, 20], electro-optics [21, 22], mechanical Kerr Effect [23], and Kerr nonlinear effect [24, 25]. For simplicity, in **Table S1** we choose two representative studies for each of these mechanisms.

Our work based on photo-thermal reduction of 2D GO films provides a new mechanism for realizing nonreciprocal light transmission. Benefitting from the broadband response of 2D GO films and the non-resonant device structure, our devices offer a considerably broader operation bandwidth (~30 nm in experimental demonstration and several hundreds of nanometers in principle) that has not been achieved previously. Moreover, our devices are fully passive, and feature a simpler device configuration that does not rely on complex external sources to generate the electric or magnetic driven fields. In contrast to the difficulties in achieving on-chip integration of magneto-optic materials [16, 25], the facile solution-based GO synthetic processes and the layer-by-layer film coating method show a high compatibility with CMOS fabrication and enable on-chip integration of 2D GO films with precise control [26, 27]

Table S1. Performance comparison of integrated non-reciprocal light transmission devices. MRR: microring resonators. MZI: Mach-Zehnder interferometer. OMC: optomechanical cavity. WG: waveguide. NTR: Non-reciprocal transmission ratio. OB: operation bandwidth.

Device structure	Mechanism	Maximum NTR	OB[1]	External drive	Function as isolator	Ref.
MRR	Magneto-optics	~19.5 dB	<0.1 nm	Yes	Yes	[13]
MRR	Magneto-optics	~32 dB	~10 nm	Yes	Yes	[14]
MRRs	Thermo-optics	~28 dB	<0.2 nm	No	No	[15]
MRR	Thermo-optics	~30 dB	<0.2 nm	No	No	[16]
MZI	Synthetic magnetic	~2.4 dB	~20 nm	Yes	Yes	[17]
OMCs	Synthetic magnetic	~35 dB	<0.01 nm	Yes	Yes	[18]
MRR	Acousto-optics	~10 dB	<0.01 nm	Yes	Yes	[20]
MRR	Acousto-optics	~39 dB	<0.01 nm	Yes	Yes	[19]
WG	Acousto-optics	~16 dB	~0.8 nm	Yes	Yes	[28]
WG	Electro-optics	~3 dB	~1.6 nm	Yes	Yes	[21]
MRRs	Electro-optics	~40 dB	<0.1 nm	Yes	Yes	[22]
MRR	Mechanical Kerr Effect	~23 dB	<0.2 nm	No	No	[23]
MRR	Kerr nonlinear effect	~20 dB	<0.2 nm	No	Yes	[24]
MRR	Kerr nonlinear effect	~17 dB, ~35 dB[2]	<0.1 nm	No	Yes	[25]
WG	Photo-thermal reduction of 2D GO	~10 dB	>>30 nm[3]	No	No	This work

[1] Here the OB is defined as the bandwidth within which the NTR is ≥ 10 dB.

[2] Here 17 dB and 35 dB correspond to the results for a single MRR and two cascaded MRRs.

[3] The operation bandwidth is limited by the amplification bandwidth of the optical amplifier in the experimental demonstrations. In principle, the broadband response of 2D GO films can span across infrared wavelengths and even extend into the visible range.

Supplementary Note 12: Calculation of GO film lengths with different reduction behaviors

In **Fig. 6a**, the GO film is divided into three segments with lengths of $L_{PR\text{-}GO}$, $L_{RR\text{-}GO}$, and $L_{NR\text{-}GO}$, which exhibit permanent reduction (PR), reversible reduction (RR), and no reduction (NR) behaviors, respectively. Here, we discuss the approach used to calculate the lengths of $L_{PR\text{-}GO}$, $L_{RR\text{-}GO}$, and $L_{NR\text{-}GO}$ based on the experimental results, using the hybrid waveguide with a monolayer of GO at a coating length of L_c = ~1.0 mm as an example.

For input power P_{in} below ~8 dBm, light propagation through the hybrid waveguide with a monolayer of GO had a constant loss of ~2.9 dB. The loss was induced by the linear loss of the Si waveguide (with a propagation loss of ~0.3 dB/mm and a total length of ~3.0 mm) and the additional loss induced by the GO film (with an excess propagation loss of ~2.0 dB/mm and a total length of ~1.0 mm). In this case, only unreduced GO is present, where $L_{UR\text{-}GO}$ equals L_c, while $L_{PR\text{-}GO}$ and $L_{RR\text{-}GO}$ are both equal to 0.

For P_{in} ranging between P_{thres1} and P_{thres2}, which are the lower and upper power thresholds for reversible photo-thermal changes, a portion of the GO film at the start exhibited RR behavior, while the remaining section retained the NR behavior. In this case, $L_{PR\text{-}GO}$ equals to 0, and the sum of $L_{RR\text{-}GO}$ and $L_{UR\text{-}GO}$ equals to L_c. As illustrated in **Fig. S10**, an input light with a power of P_{in} (dBm) first experiences a constant loss of 0.3 dB/mm × 1.0 mm = 0.3 dB before reaching the start of the GO-coated section. In the GO coated section, the light power at the start of the NR-GO segment is P_{thres1} - 0.3 dB. This is because, according to the experimental results in **Fig. 3** and **4**, P_{thres1} is determined by the GO film properties and remains consistent despite variations in L_c. The subtraction of 0.3 dB from P_{thres1} is because P_{thres1} represents the measured input power to the hybrid waveguide in our experiment (*i.e.*, at L = 0 mm in **Fig. S10**), and the actual power reaching the GO coated section (*i.e.*, at L = 1 mm in **Fig. S10**) needs to be reduced by 0.3 dB from this value. In the NR-GO segment, the light experiences a constant linear propagation loss of 0.3 dB/mm + 2.0 dB/mm = 2.3 dB/mm. Subsequently, the output from the GO-coated section encountered a constant loss of ~0.3 dB before reaching the waveguide output. Considering the above processes, it can be deduced that:

$$(P_{thres1} - 0.3) - 2.3 \times L_{NR\text{-}GO} - 0.3 = P_{out} \quad \text{(S6)}$$

where P_{out} is the measured output power from the hybrid waveguide. According to **Eq. (S6)**, for a given input power P_{in} (dBm) ranging between P_{thres1} and P_{thres2}, $L_{NR\text{-}GO}$ can be calculated by

$$L_{NR\text{-}GO} = (P_{thres1} - 0.6 - P_{out}) / 2.3 \tag{S7}$$

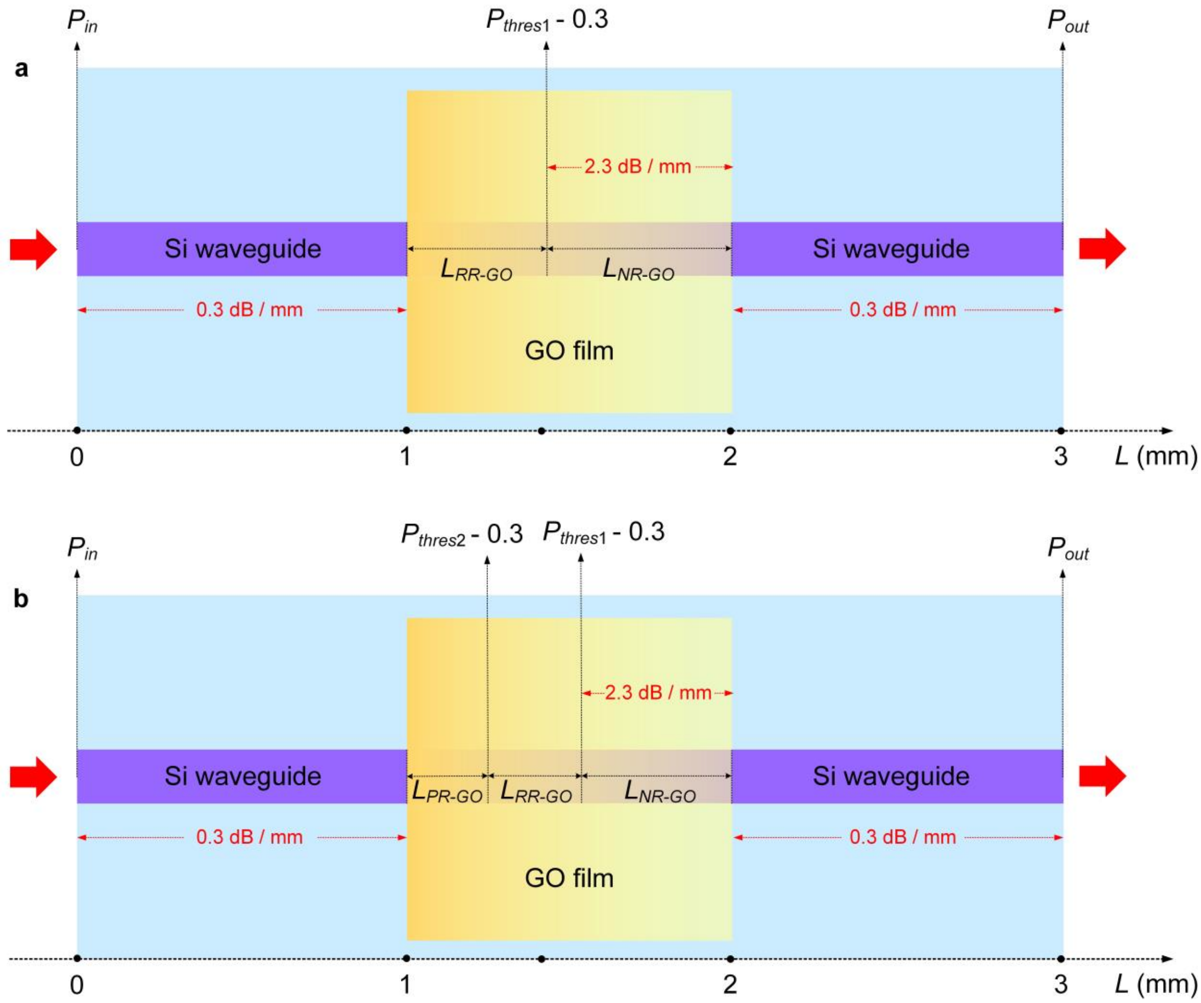

Fig. S10 | Schematic illustration showing propagation loss of different parts of the hybrid waveguide with a monolayer of GO. **a.** For an input power P_{in} in the range between P_{thres1} and P_{thres2}, the GO film is divided into two segments corresponding to reversible reduction (RR), and no reduction (NR), with lengths denoted as $L_{RR\text{-}GO}$ and $L_{NR\text{-}GO}$, respectively. **b.** For P_{in} exceeding P_{thres2}, The GO film is divided into three segments corresponding to permanent reduction (PR), RR, and NR, with respective lengths denoted as $L_{PR\text{-}GO}$, $L_{RR\text{-}GO}$, and $L_{NR\text{-}GO}$. In **a** and **b**, P_{thres1} and P_{thres2} denote the lower and upper power thresholds for the reversible photo-thermal changes, respectively. All power values are expressed in the unit of dBm. The propagation loss for the uncoated Si waveguide and the NR-GO segment are 0.3 dB / mm and 2.3 dB / mm, respectively.

Given the relation between $L_{NR\text{-}GO}$ and $L_{RR\text{-}GO}$ in this power range, $L_{RR\text{-}GO}$ can be calculated by

$$L_{RR\text{-}GO} = L_c - L_{NR\text{-}GO} \tag{S8}$$

For example, for P_{in} = P_{thres2} = 19.2 dBm, the measured output power was ~6.1 dBm. Considering that P_{thres1}= 8.0 dBm for the hybrid waveguide with a monolayer of GO, we can obtain that $L_{NR\text{-}GO}$ = (8.0 - 0.6 - 6.1) / 2.3 = 0.57 mm, and subsequently, $L_{RR\text{-}GO}$ = 1.0 - 0.57 = 0.43 mm.

When P_{in} exceeds P_{thres2}, there exists permanently reduced GO, meaning that $L_{PR\text{-}GO}$ is no longer equal to 0. In this scenario, the power first decreases to P_{thres2} - 0.3 dB after going through the PR-GO segment, and subsequently decreases to P_{thres1} - 0.3 dB after passing the RR-GO segment. Following this, it experiences a constant propagation loss of 2.3 dB / mm in the NR-GO segment. According to the above processes, $L_{NR\text{-}GO}$ can still be calculated based on **Eq. (S7)**, while $L_{RR\text{-}GO}$ remains fixed at 0.43 nm, corresponding to the value derived for P_{in} = P_{thres2} as discussed previously. Therefore, $L_{PR\text{-}GO}$ can be calculated by

$$L_{PR\text{-}GO} = L_c - L_{NR\text{-}GO} - L_{RR\text{-}GO} \tag{S9}$$

Although the propagation loss is non-uniform and varies with the reduction degree in both the PR-GO and RR-GO segments, the method mentioned above allows us to calculate the respective lengths of these segments. This serves as the basis for our subsequent extraction and analysis of material properties for the permanently and reversibly reduced GO films.

Supplementary Note 13: Calculation of power evolution along the hybrid waveguides

In the uncoated Si segment and the NR-GO segment with a constant propagation loss of 0.3 dB / mm and 2.3 dB / mm, respectively, the power experiences exponential decay, making it straightforward to calculate the power evolutions. Therefore, here we focus on discussing the approach to calculate the power evolution along the RR-GO and PR-GO segments.

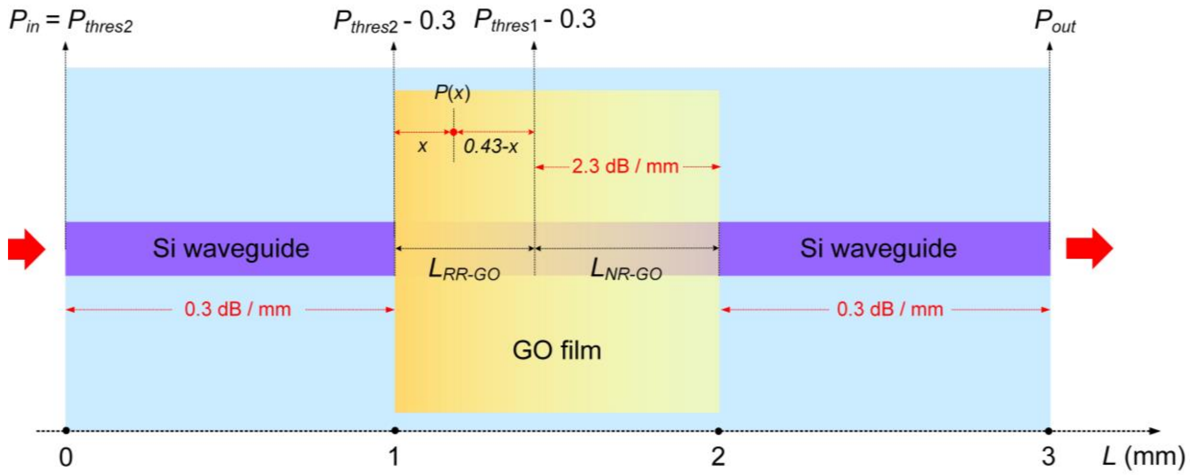

Fig. S11 | Schematic illustration showing calculation of power evolution along the RR-GO segment. For an input power $P_{in} = P_{thres2}$, the GO film is divided into RR-GO and NR-GO segments with lengths of L_{RR-GO} = 0.43 nm and L_{NR-GO} = 0.57 nm, respectively. $P(x)$ denotes the light power as a function of the length along the GO film, where $0 \leq x \leq 0.43$.

As discussed in **Note 12**, for a given input power P_{in}, the corresponding L_{PR-GO}, L_{RR-GO}, and L_{NR-GO} can be calculated based on **Eqs. (S6) – (S9)**. For example, when $P_{in} = P_{thres2}$, only the RR-GO and NR-GO segments are present, and the calculated L_{RR-GO} is 0.43 mm. As shown in **Fig. S11**, in order to calculate the power evolution along the RR-GO segment, we represent the light power as a function of the length along the GO film, denoted as $P(x)$, where $0 \leq x \leq$ 0.43 mm. Assuming that the loss of the reversibly reduced GO is only influenced by the light power injected into the waveguide cross-section, the length of the RR-GO segment from $P(x)$ to the end (with a length of 0.43-x) should be the same as the L_{RR-GO} calculated for an input power of $P(x)$ + 0.3 (dBm). In other words, for an input power of $P_{in} = P(x)$ + 0.3 (dBm), the calculated L_{RR-GO} based on the approach discussed in **Note 12** should be 0.43-x. Note that the input power we are referring to here is the power injected at the start of the Si waveguide (*i.e.*, L = 0 mm in **Fig. S11**). Therefore, it was adjusted based on $P(x)$ by adding a 0.3-dB loss along the uncoated Si waveguide before reaching the GO-coated section.

According to the above discussion, for a given input power P_{in}, the corresponding $P(x) = P_{in} - 0.3$ and $x = 0.43 - L_{RR\text{-}GO}$ can be calculated. By performing a polynomial fit on the relationship between the obtained x and $P(x)$, using data calculated for various P_{in} values, we obtained a curve showing the relation between x and $P(x)$, as depicted in **Fig. S12**. This curve reflects the power evolution along the RR-GO segment.

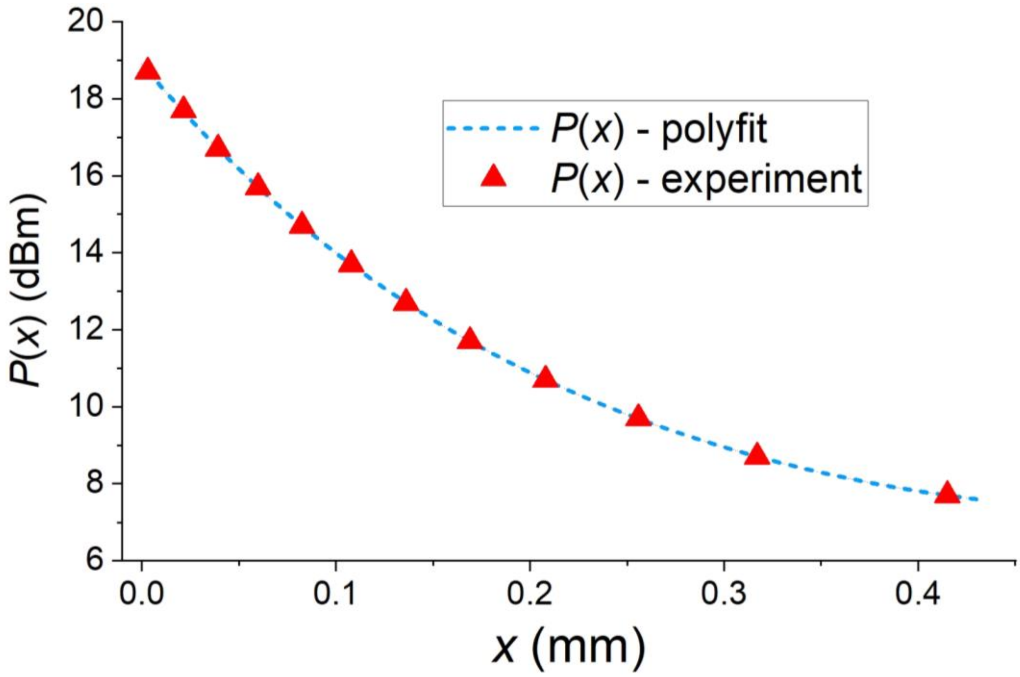

Fig. S12 | Relationship between x and $P(x)$ in **Fig. S11**. For an input power P_{in} in the range between P_{thres1} and P_{thres2}, the corresponding $L_{RR\text{-}GO}$ can be calculated from experimental results based on **Eqs. (S6) – (S8)**. This yields a pair of values (x, $P(x)$), where $x = 0.43\text{-} L_{RR\text{-}GO}$ and $P(x) = P_{in} - 0.3$. The curve was generated by conducting a polynomial fit on the relationship between x and $P(x)$, using the data points obtained for various P_{in} values (indicated as red triangles).

For $P_{in} > P_{thres2}$, there exists permanently reduced GO, and so the GO film can be divided into PR-GO, RR-GO, NR-GO segments. In this case, $L_{RR\text{-}GO}$ remains constant at 0.43 mm and the power evolution along the RR-GO segment is consistent with that for $P_{in} = P_{thres2}$. In the PR-GO segment, the power evolution can be obtained using the same approach previously discussed for obtaining the power evolution along the RR-GO segment.

Based on the approach discussed above, we calculated the power evolution along the hybrid waveguide for four different input power levels across various power ranges and illustrates the results in **Fig. 6c**.

Supplementary Note 14: Extracting extinction coefficient of photo-thermally reduced GO

Prior to extracting the extinction coefficient of photo-thermally reduced GO, we first calculated the propagation loss of the GO-Si hybrid waveguides. In both the uncoated Si segment and the NR-GO segment, the propagation loss remains constant at 0.3 dB/mm and 2.3 dB/mm, respectively. For the NR-GO and PR-GO segments, the propagation loss can be expressed as a function of the input light power, and it can be calculated by taking the derivative of the power evolution shown in **Fig. 6c**. In **Fig. 6d**, the calculated propagation loss for the GO-coated waveguides is plotted as a function of $P_{in,\ hybrid}$, where $P_{in,\ hybrid}$ is the light power injected into the hybrid waveguide cross-section. Assuming that the loss induced by the GO film is determined by the light power injected into the waveguide cross-section, $P_{in,\ hybrid}$ is directly related to the power-dependent propagation loss of the hybrid waveguides.

Based on the propagation loss of the hybrid waveguides, we calculated the corresponding imaginary part of the waveguide refractive index n_i based on the following equations [11, 29]:

$$a = exp(-2\pi \cdot n_i \cdot L/\lambda) \tag{S10}$$

$$PL - 0.3 = -10 \cdot log_{10}(a^2) \tag{S11}$$

where a is the amplitude of the optical field, L = 1.0 mm is the waveguide length, λ is the light wavelength, and PL is the propagation loss in the unit of dB/mm. In **Eq. (S11)**, the squaring of a is performed to convert the field amplitude into the corresponding optical intensity. The subtraction of 0.3 dB/mm is done to exclude the propagation loss of the uncoated Si waveguide. By substituting **Eq. (S11)** into **Eq. (S10)**, n_i can be expressed as

$$n_i = ln\left[10^{\frac{-(PL - 0.3)}{20}}\right] \cdot \frac{-\lambda}{2\pi \cdot 10^{-3}} \tag{S12}$$

Finally, we obtained the fitted extinction coefficient, k_{GO}, for the 2D GO films by employing commercial mode solving software. This involved adjusting k_{GO} to ensure that the simulated imaginary part of the waveguide effective index aligned with the value of n_i calculated through **Eqs. (S10)** – **(S12)** (assuming extinction coefficients for other materials were 0). By repeating the above processes, we obtained the fitted k_{GO} values for various $P_{in,\ hybrid}$ levels and depicted them in **Fig. 6d**.

Supplementary Note 15: Thermal simulations for the hybrid waveguides

The steady-state temperature profiles within the waveguide cross-section were simulated using commercial software (COMSOL Multiphysics®) based on the finite-element method (FEM). To calculate the heat power density required for thermal simulation, the optical waveguide was treated as a conductor with a high resistance. Based on the vector form of the *Ohm*'s law used in electromagnetics and material science [30], the relationship between the electrical current density and the electric field can be expressed as:

$$\boldsymbol{J} = \sigma \boldsymbol{E} \tag{S13}$$

where $\boldsymbol{J}$ and $\boldsymbol{E}$ are the vectors for the current density and electric field, respectively. In **Eq. (S13)**, σ represents the material-specific electrical conductivity (in the unit of S/m), which is the reciprocal of electrical resistivity ρ. For a conductor with length L, cross-sectional area A, and electrical resistivity ρ, the heat power generated by the electrical current passing through it can be given by:

$$P_{thermal} = I^2 R = (JA)^2 \frac{\rho L}{A} = J^2 \rho A L \tag{S14}$$

where $P_{thermal}$ is the heat power, I is the electrical current, and R is the electrical resistance. By substituting **Eq. (S13)** into **Eq. (S14)**, and considering that $\sigma \cdot \rho = 1$, **Eq. (S14)** can be simplified as:

$$P_{thermal} = \sigma E^2 A L \tag{S15}$$

Hence, the heat power density, denoted as $Q_{thermal}$ and defined as the heat power within a unit volume, can be expressed as:

$$Q_{thermal} = \frac{P_{thermal}}{AL} = \sigma E^2 \tag{S16}$$

For time-varying electromagnetic fields like an optical field, **Eq. (S16)** can be reformulated as:

$$Q_{thermal,\ avg} = \frac{1}{2} \sigma E_0^2 \tag{S17}$$

where $Q_{thermal,avg}$ is the time-averaged heat power density, and E_0 is the amplitude of the optical field.

According to classical electromagnetic field and wave theory, the energy density of an electromagnetic field propagating in a dielectric medium can be expressed as [31]:

$$Q_{EM} = \frac{1}{2}\varepsilon E_0^2 \tag{S18}$$

where Q_{EM} is the energy density and ε is permittivity of the medium. In the context of optical waveguides, the energy of light passing through the waveguide cross section during a time interval of Δt can be given by

$$W = Q_{EM} \cdot V = \frac{Q_{EM} \cdot A \cdot \Delta t \cdot c}{n} \tag{S19}$$

where V is the volume through which light propagates, A is the cross-sectional area, and c/n is the speed of light propagating in the waveguide, with c denoting the speed of light in vacuum and n the effective refractive index of the waveguide. Based on **Eq. (S19)**, the light intensity on the waveguide cross section, which is defined as the light power on a unit area, can be written as:

$$I = \frac{P}{A} = \frac{W}{A \cdot \Delta t} = \frac{Q_{EM} \cdot c}{n} = \frac{\varepsilon \cdot E_0^2 \cdot c}{2n} \tag{S20}$$

where P is the total light power within the waveguide cross-section. By substituting **Eq. (S20)** into **Eq. (S17)** and eliminating E_0, $Q_{thermal,avg}$ can be rewritten as

$$Q_{thermal,\ avg} = \frac{P \cdot \sigma \cdot n}{\varepsilon \cdot c \cdot A} \tag{S21}$$

Using **Eq. (S21)**, the heat power density in a uniform optical waveguide can be calculated for a given input power P. For a hybrid waveguide, different material regions act as different heat sources. In this case, **Eq. (S21)** can be modified based on the optical mode distribution to calculate the heat power density within a particular material region as follows:

$$Q_{thermal,\ avg} = \frac{P \cdot \eta \cdot \sigma \cdot n}{\varepsilon \cdot c \cdot A} \tag{S22}$$

where η is the optical mode overlap with the material region, and P is the overall light power in the waveguide cross section. Given the relation between n and ε given by [31]

$$n = \sqrt{\varepsilon \cdot \mu} \tag{S23}$$

and assuming that all the materials in the waveguide cross section are non-magnetic materials with a permeability μ =1, **Eq. (S22)** can be simplified as:

$$Q_{thermal,\ avg} = \frac{P \cdot \eta \cdot \sigma}{n \cdot c \cdot A} \tag{S24}$$

In **Eq. (S24)**, σ and n represent the material property parameters associated with the specific material region, and A denotes the area of the material region in the waveguide cross section.

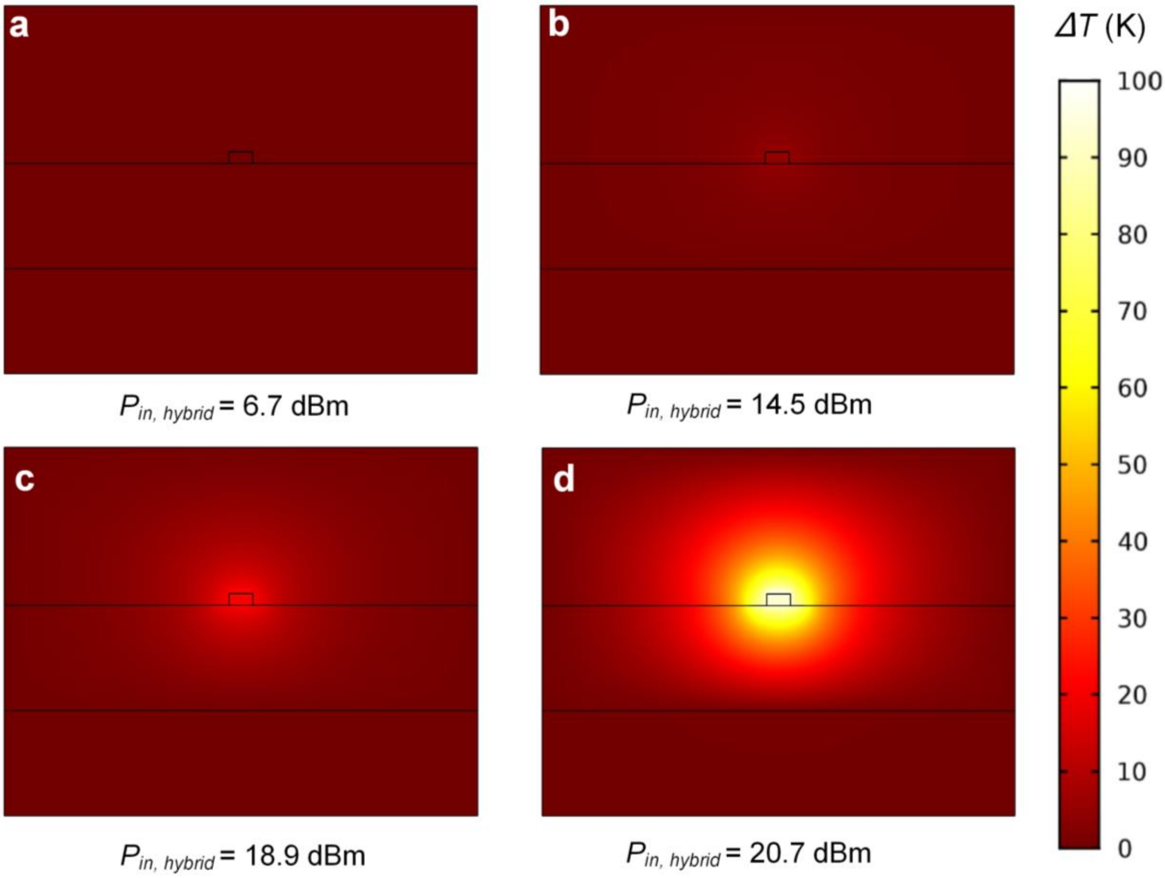

Fig. S13 | Simulated temperature profiles in cross section of the hybrid waveguide with a monolayer of GO at different $P_{in,\ hybrid}$, which are the input powers injected into the waveguide cross-section. **a.** $P_{in,\ hybrid}$ = 6.7 dBm. **b.** $P_{in,\ hybrid}$ = 14.5 dBm. **c.** $P_{in,\ hybrid}$ = 18.9 dBm. **d.** $P_{in,\ hybrid}$ = 20.7 dBm.

In the FEM thermal simulation software, we set the heat power densities in different material regions to match the values calculated using **Eq. (S22)** and specified the thermal conductivities for each of the material regions. This allowed us to obtain the steady-state temperature profiles within the cross-sections of the hybrid waveguides.

Fig. S13 shows the temperature profiles in the cross section of the hybrid waveguide with a monolayer of GO, with simulations conducted at various input powers injected into the waveguide cross-section (*i.e.*, $P_{in,\ hybrid}$), as described previously. The corresponding zoom-in views with marked isotherms are provided in **Fig. S14.** In our simulation, the optical mode overlap η was calculated using FDTD mode simulation software. The values of the thermal conductivities for air, silicon, and silica used were 0.025, 149, and 1.4 $Wm^{-1}K^{-1}$ [32, 33], respectively. The thermal conductivity for unreduced GO was 25.6 $Wm^{-1}K^{-1}$, which was obtained from our previous measurements of GO films prepared using the same method [34, 35]. The values of the thermal conductivities for the reduced GO at various $P_{in,\ hybrid}$ were obtained by fitting the experimentally measured temperature variation with theoretical simulations, as elaborated in detail in **Note 16**. The simulation results also show that the polymer-GO-polymer sandwiched films structure (as shown in **Fig. S6a-IV**) hampers heat dissipation and augments the temperature within the GO film.

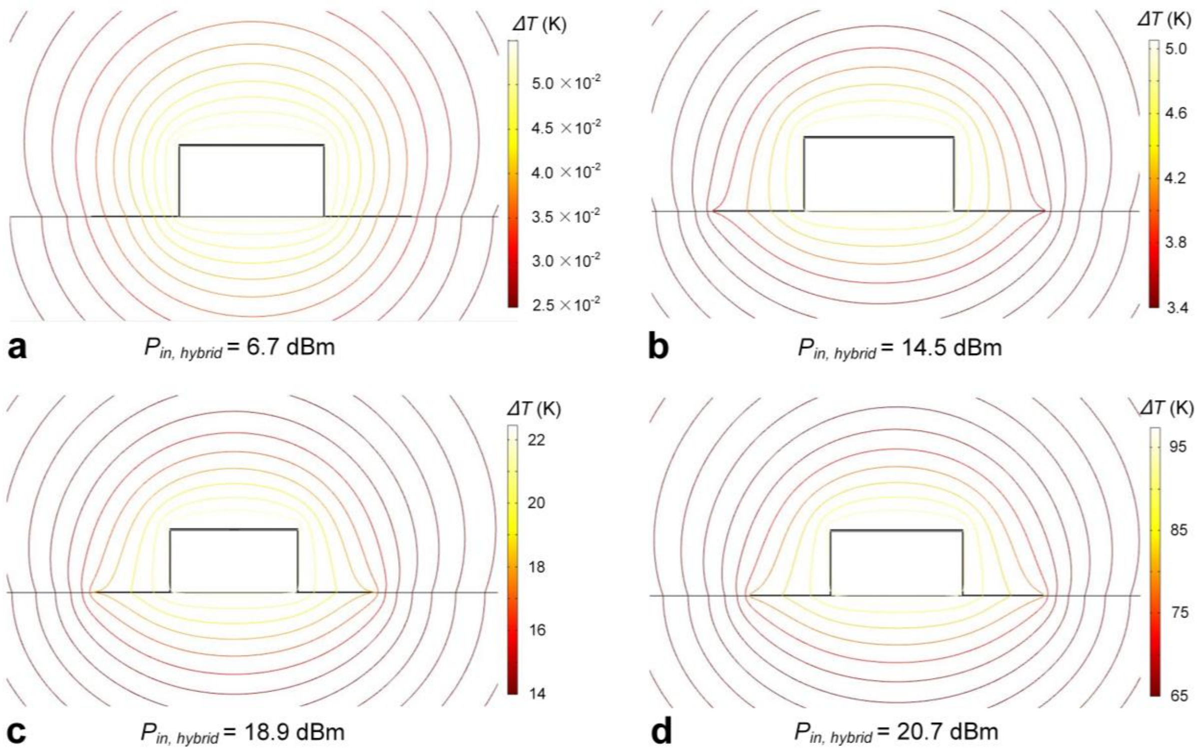

Fig. S14 | Zoom-in view of the temperature profiles in **Fig. S13**. The lines indicating equal temperatures (isotherms) are highlighted.

Supplementary Note 16: Extraction of thermal conductivities and calculation of temperature changes

As illustrated in **Fig. S15**, in the same plane perpendicular to the light propagation direction, there are two points denoted as *A* and *B*. In our experiment, the temperature probe was positioned at point *A*, which was situated at a distance of ~2.5 μm from the bottom of the Si waveguide. Point *B* is located within the GO film, and its proximity to the heat sources results in a higher temperature compared to that at Point *A*.

First, we simulated the temperature at point *A* for a hybrid waveguide with unreduced GO, denoted as $T_{A,\ GO}$, using the FEM thermal simulation software. The heat power densities at different material regions were calculated based on **Eq. (S22)** discussed in **Note 15**, using the thermal conductivities of Si and unreduced GO. By properly setting the simulation area and boundary temperature, $T_{A,\ GO}$ was adjusted to be consistent with the measured value in the experiment.

Subsequently, we obtained the thermal conductivity for the reduced GO film by fitting the measured temperature difference ΔT between the reduced and unreduced GO segments. This involved adjustment of the thermal conductivity of the GO region in the FEM thermal simulation software, denoted as K_{GO}, to ensure that the simulated temperature variation at point *A* equals to $T_{A,\ GO} + \Delta T$. In the fitting process, we neglected the slight difference in *n* and *A* between the unreduced and reduced GO when calculating the heat power density in the GO region using **Eq. (S24)**. According to classical electromagnetic field and wave theory, the relationship between a material's electrical conductivity and its relative permittivity can be given by [36]:

$$\varepsilon_r = \varepsilon_r + i \cdot \varepsilon_i = \varepsilon_r + i \cdot \frac{\sigma}{\omega} \tag{S25}$$

where ε is the complex permittivity, with ε_r and ε_i denoting its real and imaginary parts, respectively. σ is the electrical conductivity and ω is the angular frequency. Therefore, it can be deduced that

$$\frac{\sigma_{RGO}}{\sigma_{GO}} = \frac{\varepsilon_{i,\ RGO}}{\varepsilon_{i,\ GO}} = \frac{Im\,[(n_{RGO} + i \cdot k_{RGO})^2]}{Im\,[(n_{GO} + i \cdot k_{GO})^2]} = \frac{2n_{RGO}k_{RGO}}{2n_{GO}k_{GO}} \approx \frac{k_{RGO}}{k_{GO}} \tag{S26}$$

where σ_{GO}, $\varepsilon_{i,GO}$, n_{GO}, and k_{GO} are the electrical conductivity, imaginary part of the permittivity, refractive index, and extinction coefficient of unreduced GO, respectively. σ_{RGO}, $\varepsilon_{i,RGO}$, n_{RGO}, and k_{RGO} are the corresponding parameters for reduced GO, respectively. In **Eq. (S26)**, we neglect the slight difference between n_{GO} and n_{RGO}. At a certain $P_{in,\ hybrid}$ that corresponding to a specific degree of reduction, σ_{RGO} was calculated based on **Eq. (S26)**, using a σ_{GO} obtained from our previous measurements [34, 35] and the data from **Fig. 6d** for k_{GO} and k_{RGO}. The calculated σ_{RGO} was employed to further calculate the corresponding heat power density based on **Eq. (S24)**. When calculating the heat power density, the difference between the input power injected into the reduced and unreduced GO segments was also considered. By repeating the above fitting processes, we obtained the fitted K_{GO} values for various $P_{in,\ hybrid}$ levels (which correspond to different degrees of reduction) and depicted them in **Fig. 6f**.

Finally, by using the fitted K_{GO} values for various $P_{in,\ hybrid}$, we calculated the corresponding temperature variations at point B, using the same simulation software. Since this point is situated within the GO films, it can serve as an indicator of temperature changes for the photo-thermal effects in GO.

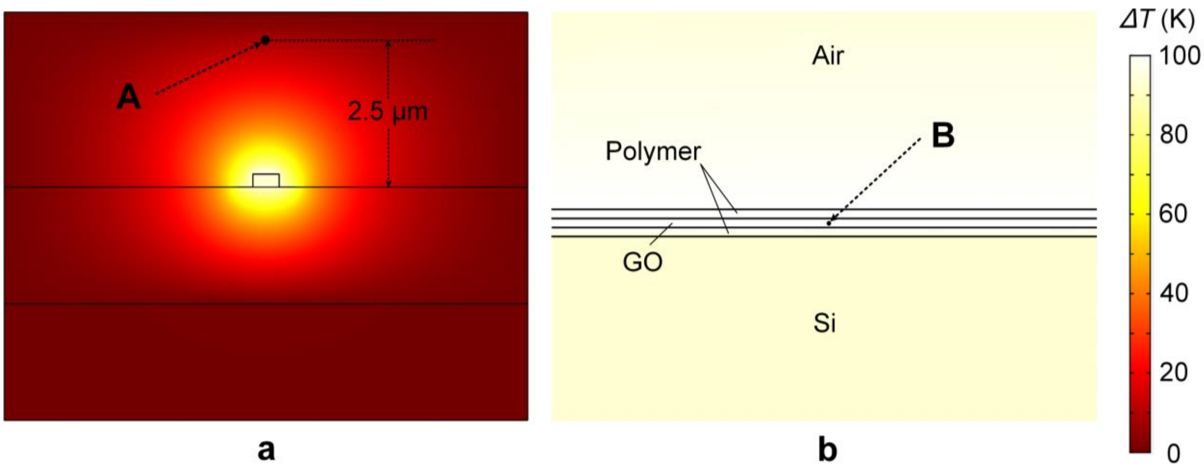

Fig. S15 | a. Simulated temperature profiles in cross section of the hybrid waveguide with a monolayer of GO at $P_{in,\ hybrid}$ = 20.7 dBm. **b.** Zoom-in view of **a** around the GO film. In **a** and **b**, points A and B represent two different positions within the waveguide cross section. The location of Point A is consistent with that of the temperature probe in our experiment. Point B is situated within the GO film.

Supplementary Note 17: Influence of GO films coated on sidewalls of Si waveguides

As shown in **Fig. S16a**, our self-assembly GO film coating method allows for conformal coating of 2D GO films onto Si waveguides, covering both their top surfaces and sidewalls. **Fig. S16b** shows the ratio of the power in GO on both sidewalls to that in all of the GO material regions, which was calculated for TE polarization using FDTD mode simulation software. As can be seen, the ratio remains below 3% for all the different GO layer numbers (*N*) employed in our device fabrication. This suggests that the mode overlap with GO on the sidewalls is minimal compared to that on the waveguide's top surface.

In principle, GO films conformally coated on the sidewalls interact with the waveguide's evanescent field in an out-of-plane manner. Nevertheless, due to the minimal mode overlap with GO on the sidewalls compared to that on the waveguide's top surface, our thermal simulations, as described in **Notes 15** and **16**, did not account for the variations in material properties arising from the anisotropy of 2D layered GO films, including parameters such as the extinction coefficient and thermal conductivity.

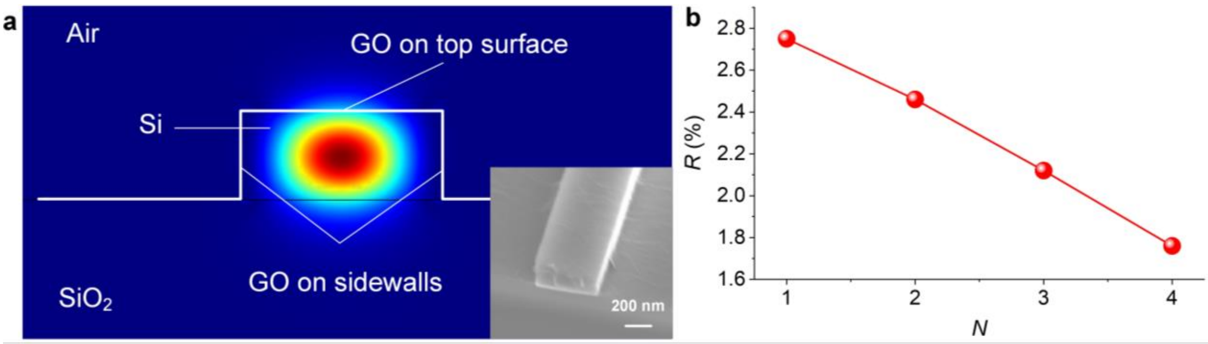

Fig. S16 | a. Simulated TE mode profile of Si waveguide conformally coated with a monolayer of GO. Inset shows a scanning electron microscope (SEM) image of a fabricated GO-Si waveguide. **b.** Ratio of power in GO coated on both sidewalls to that in all GO material regions (*R*) as a function of GO layer number (*N*).

References

[1] L. Yin, and G. P. Agrawal, "Impact of two-photon absorption on self-phase modulation in silicon waveguides," *Optics Letters,* vol. 32, no. 14, pp. 2031-2033, 2007/07/15, 2007.

[2] G. Shiming, L. Zhiqiang, T. En-Kuang, H. Sailing, and O. Boyraz, "Performance Evaluation of Nondegenerate Wavelength Conversion in a Silicon Nanowire Waveguide," *Journal of Lightwave Technology*, 2010.

[3] J. Leuthold, C. Koos, and W. Freude, "Nonlinear silicon photonics," *Nature Photonics,* vol. 4, no. 8, pp. 535-544, 2010.

[4] A. V. Dolbin, M. V. Khlistyuck, V. B. Esel'son, V. G. Gavrilko, N. A. Vinnikov, R. M. Basnukaeva, I. Maluenda, W. K. Maser, and A. M. Benito, "The effect of the thermal reduction temperature on the structure and sorption capacity of reduced graphene oxide materials," *Applied Surface Science,* vol. 361, pp. 213-220, 2016.

[5] Y. C. Guan, Y. W. Fang, G. C. Lim, H. Y. Zheng, and M. H. Hong, "Fabrication of Laser-reduced Graphene Oxide in Liquid Nitrogen Environment," *Sci Rep,* vol. 6, pp. 28913, Jun 27, 2016.

[6] P. J. Winzer, and R.-J. Essiambre, "Advanced optical modulation formats," *Optical Fiber Telecommunications VB*, pp. 23-93: Elsevier, 2008.

[7] R. Zhang, Y. He, Y. Zhang, S. An, Q. Zhu, X. Li, and Y. Su, "Ultracompact and low-power-consumption silicon thermo-optic switch for high-speed data," *Nanophotonics,* vol. 10, no. 2, pp. 937-945, 2020.

[8] Y. Qu, J. Wu, Y. Yang, Y. Zhang, Y. Liang, H. El Dirani, R. Crochemore, P. Demongodin, C. Sciancalepore, C. Grillet, C. Monat, B. Jia, and D. J. Moss, "Enhanced Four-Wave Mixing in Silicon Nitride Waveguides Integrated with 2D Layered Graphene Oxide Films," *Advanced Optical Materials,* vol. 8, no. 23, pp. 2001048, 2020/12/01, 2020.

[9] J. Wu, Y. Yang, Y. Qu, L. Jia, Y. Zhang, X. Xu, S. T. Chu, B. E. Little, R. Morandotti, B. Jia, and D. J. Moss, "2D Layered Graphene Oxide Films Integrated with Micro-Ring Resonators for Enhanced Nonlinear Optics," *Small,* vol. 16, no. 16, pp. 1906563, 2020/04/01, 2020.

[10] Y. Zhang, J. Wu, Y. Yang, Y. Qu, L. Jia, T. Moein, B. Jia, and D. J. Moss, "Enhanced Kerr Nonlinearity and Nonlinear Figure of Merit in Silicon Nanowires Integrated with 2D Graphene Oxide Films," *ACS Applied Materials & Interfaces,* vol. 12, no. 29, pp. 33094-33103, 2020/07/22, 2020.

[11] J. Wu, Y. Yang, Y. Qu, X. Xu, Y. Liang, S. T. Chu, B. E. Little, R. Morandotti, B. Jia, and D. J. Moss, "Graphene Oxide Waveguide and Micro-Ring Resonator Polarizers," *Laser & Photonics Reviews,* vol. 13, no. 9, pp. 1900056, 2019/09/01, 2019.

[12] H. Lin, Y. Song, Y. Huang, D. Kita, S. Deckoff-Jones, K. Wang, L. Li, J. Li, H. Zheng, Z. Luo, H. Wang, S. Novak, A. Yadav, C.-C. Huang, R.-J. Shiue, D. Englund, T. Gu, D. Hewak, K. Richardson, J. Kong, and J. Hu, "Chalcogenide glass-on-graphene photonics," *Nature Photonics,* vol. 11, no. 12, pp. 798-805, 2017.

[13] L. Bi, J. Hu, P. Jiang, D. H. Kim, G. F. Dionne, L. C. Kimerling, and C. A. Ross, "On-chip optical isolation in monolithically integrated non-reciprocal optical resonators," *Nature Photonics,* vol. 5, no. 12, pp. 758-762, 2011.

[14] W. Yan, Y. Yang, S. Liu, Y. Zhang, S. Xia, T. Kang, W. Yang, J. Qin, L. Deng, and L. Bi, "Waveguide-integrated high-performance magneto-optical isolators and circulators on silicon nitride platforms," *Optica,* vol. 7, no. 11, pp. 1555-1562, 2020/11/20, 2020.

[15] L. Fan, J. Wang, L. T. Varghese, H. Shen, B. Niu, Y. Xuan, A. M. Weiner, and M. H. Qi, "An All-Silicon Passive Optical Diode," *Science,* vol. 335, no. 6067, pp. 447-450, Jan 27, 2012.

[16] A. Li, and W. Bogaerts, "Reconfigurable nonlinear nonreciprocal transmission in a silicon photonic integrated circuit," *Optica,* vol. 7, no. 1, pp. 7, 2020.

[17] L. D. Tzuang, K. Fang, P. Nussenzveig, S. Fan, and M. Lipson, "Non-reciprocal phase shift induced by an effective magnetic flux for light," *Nature Photonics,* vol. 8, no. 9, pp. 701-705, 2014.

[18] K. Fang, J. Luo, A. Metelmann, M. H. Matheny, F. Marquardt, A. A. Clerk, and O. Painter, "Generalized non-reciprocity in an optomechanical circuit via synthetic magnetism and reservoir engineering," *Nature Physics,* vol. 13, no. 5, pp. 465-471, 2017.

[19] D. B. Sohn, O. E. Örsel, and G. Bahl, "Electrically driven optical isolation through phonon-mediated photonic Autler–Townes splitting," *Nature Photonics*, 2021.

[20] H. Tian, J. Liu, A. Siddharth, R. N. Wang, T. Blésin, J. He, T. J. Kippenberg, and S. A. Bhave, "Magnetic-free silicon nitride integrated optical isolator," *Nature Photonics,* vol. 15, no. 11, pp. 828-836, 2021.

[21] H. Lira, Z. Yu, S. Fan, and M. Lipson, "Electrically driven nonreciprocity induced by interband photonic transition on a silicon chip," *Phys Rev Lett,* vol. 109, no. 3, pp. 033901, Jul 20, 2012.

[22] J. F. Herrmann, V. Ansari, J. Wang, J. D. Witmer, S. Fan, and A. H. Safavi-Naeini, "Mirror symmetric on-chip frequency circulation of light," *Nature Photonics,* vol. 16, no. 8, pp. 603-608, 2022.

[23] L. Ren, X. Xu, S. Zhu, L. Shi, and X. Zhang, "Experimental Realization of on-Chip Nonreciprocal Transmission by Using the Mechanical Kerr Effect," *ACS Photonics*, 2020.

[24] K. Y. Yang, J. Skarda, M. Cotrufo, A. Dutt, G. H. Ahn, M. Sawaby, D. Vercruysse, A. Arbabian, S. Fan, A. Alù, and J. Vučković, "Inverse-designed non-reciprocal pulse router for chip-based LiDAR," *Nature Photonics,* vol. 14, no. 6, pp. 369-374, 2020.

[25] A. D. White, G. H. Ahn, K. V. Gasse, K. Y. Yang, L. Chang, J. E. Bowers, and J. Vučković, "Integrated passive nonlinear optical isolators," *Nature Photonics*, 2022.

[26] J. Wu, L. Jia, Y. Zhang, Y. Qu, B. Jia, and D. J. Moss, "Graphene Oxide for Integrated Photonics and Flat Optics," *Advanced Materials,* vol. 33, no. 3, pp. 2006415, 2021/01/01, 2021.

[27] J. Wu, H. Lin, D. J. Moss, K. P. Loh, and B. Jia, "Graphene oxide for photonics, electronics and optoelectronics," *Nature Reviews Chemistry*, 2023.

[28] E. A. Kittlaus, W. M. Jones, P. T. Rakich, N. T. Otterstrom, R. E. Muller, and M. Rais-Zadeh, "Electrically driven acousto-optics and broadband non-reciprocity in silicon photonics," *Nature Photonics,* vol. 15, no. 1, pp. 43-52, 2020.

[29] H. Arianfard, S. Juodkazis, D. J. Moss, and J. Wu, "Sagnac interference in integrated photonics," *Applied Physics Reviews,* vol. 10, no. 1, pp. 011309, 2023/03/01, 2023.

[30] X. Gu, Y. Wei, X. Yin, B. Li, and R. Yang, "Colloquium: Phononic thermal properties of two-dimensional materials," *Reviews of Modern Physics,* vol. 90, no. 4, 2018.

[31] J. G. Van Bladel, *Electromagnetic fields*: John Wiley & Sons, 2007.

[32] A. Grieco, B. Slutsky, D. T. H. Tan, S. Zamek, M. P. Nezhad, and Y. Fainman, "Optical Bistability in a Silicon Waveguide Distributed Bragg Reflector Fabry–Pérot Resonator," *Journal of Lightwave Technology,* vol. 30, no. 14, pp. 2352-2355, 2012.

[33] C. Horvath, D. Bachman, R. Indoe, and V. Van, "Photothermal nonlinearity and optical bistability in a graphene-silicon waveguide resonator," *Opt Lett,* vol. 38, no. 23, pp. 5036-9, Dec 1, 2013.

[34] H. Lin, B. C. P. Sturmberg, K.-T. Lin, Y. Yang, X. Zheng, T. K. Chong, C. M. de Sterke, and B. Jia, "A 90-nm-thick graphene metamaterial for strong and extremely broadband absorption of

unpolarized light," *Nature Photonics,* vol. 13, no. 4, pp. 270-276, 2019.

[35] K. T. Lin, H. Lin, T. Yang, and B. Jia, "Structured graphene metamaterial selective absorbers for high efficiency and omnidirectional solar thermal energy conversion," *Nat Commun,* vol. 11, no. 1, pp. 1389, Mar 13, 2020.

[36] J. D. Patterson, and B. C. Bailey, "Optical Properties of Solids," *Solid-State Physics: Introduction to the Theory*, J. D. Patterson and B. C. Bailey, eds., pp. 649-704, Cham: Springer International Publishing, 2018.